Numerical analysis of coupled transport and reaction phenomena in an anode-supported flat-tube solid oxide fuel cell

Masayuki Suzuki [a,*], Naoki Shikazono [a], Koji Fukagata [b], Nobuhide Kasagi [a]

[a] Department of Mechanical Engineering, The University of Tokyo, Hongo 7-3-1, Bunkyo-ku, Tokyo 113-8656, Japan
[b] Department of Mechanical Engineering, Keio University, Hiyoshi 3-14-1, Kohoku-ku, Yokohama 223-8522, Japan

ABSTRACT

Heat and mass transfer with electrochemical reaction in an anode-supported flat-tube solid oxide fuel cell (FT-SOFC) is studied by means of three-dimensional numerical simulation. The distributions of the reaction fields in the anode-supported FT-SOFC are found to be similar to those in the planar SOFC with co-flow arrangement. However, in comparison with the latter, the concentration and activation overpotentials of the former can be reduced by additional reactant diffusion through the porous rib of the fuel channel. Parametric survey reveals that, for a fixed activation overpotential model, the output voltage can be improved by increasing the pore size of anode, while the cross-sectional geometry has smaller effect on the cell performance. Based on the results of three-dimensional simulation, we also develop a simplified numerical model of anode-supported FT-SOFC, which takes into account the concentration gradients in the thick anode of complex cross-sectional geometry. The simplified model can sufficiently predict the output voltage as well as the distributions of temperature and current density with very low computational cost. Thus, it can be used as a powerful tool for surveying wide range of anode-supported FT-SOFC design parameters.

© 2008 Elsevier B.V. All rights reserved.

1. Introduction

Solid oxide fuel cell (SOFC) is expected to be a promising alternative power generation system with its high energy conversion efficiency, wide fuel adaptability, and possible exhaust-heat utilization [1]. Recently, a flat-tube SOFC (FT-SOFC) has attracted increasing attention among various cell configurations due to its high power density and the relative easiness of fabrication and gas sealing [2,3]. For successful implementation of SOFC, however, the cost performance should be further improved both in the manufacturing and operating processes. Therefore, development of cells with high efficiency and high power density is a current priority issue.

The performance characteristics of SOFC can be increased by reduction of overpotentials, which result from electrochemical processes in the cell. One way to reduce the overpotential is to properly manage the heat and mass transfer associated with the electrochemical reaction. In order to study such transport and reaction phenomena, numerical simulation should be helpful to obtain detailed (and experimentally unavailable) information in the cell.

In the last decade, a number of numerical studies have been reported for the detailed heat and mass transfer in SOFCs [4–7]. These studies reveal that the flow and thermal fields in the cell have three-dimensional distribution strongly depending on the design parameters of the cell components. However, most of the previous studies assume homogeneous reaction field and have not treated the coupled transport and reaction phenomena that largely affects the cell performance characteristics. Exceptionally, several recent investigations of tubular, planar, and cathode-supported FT-SOFCs [3,8–10] account for such interactive effect.

When compared to the cathode-supported FT-SOFC mentioned above, the anode-supported FT-SOFC has potential advantages due to its lower internal resistance and higher limit current [1,11], and therefore it attracts considerable attention. The anode-supported FT-SOFC has a thick anode, of which cross-sectional geometry is often complicated. Its performance is determined by the three-dimensional heat and mass transport, which may be strongly dependent on the cell design, such as the geometrical configuration and the microstructure of cell components. To the authors' knowledge, however, detailed numerical simulation of coupled transport and reaction phenomena in the anode-supported FT-SOFC has not been reported.

The purpose of the present study is to investigate the fundamental transport and reaction phenomena in an anode-supported FT-SOFC. First, we perform numerical simulation with a full 3D

* Corresponding author. Present address: Tobikoshi 5-1, Terazu, Nishio, Aichi, 444-0324, Japan. Tel.: +81 563 59 2719; fax: +81 563 59 2719.

E-mail address: msuzuki@thtlab.t.u-tokyo.ac.jp (M. Suzuki).

Nomenclature

$c_{p,i}$	molar specific heat of reactant i ($J mol^{-1} K^{-1}$)
C_p	isobaric specific heat ($J kg^{-1} K^{-1}$)
d_p	pore diameter of the electrode (m)
D_i	Diffusivity of the reactant i ($m^2 s^{-1}$)
E	electromotive force (EMF) (V)
F	Faraday constant: 9.649×10^4 ($C mol^{-1}$)
ΔG_{H_2O}	Gibbs' free-energy change accompanied by water formation ($J mol^{-1}$)
h	heat transfer coefficient ($W m^{-2} K^{-1}$)
ΔH_{H_2O}	enthalpy change accompanied by water formation ($J mol^{-1}$)
i	current density ($A m^{-2}$)
$\bar{m}_i$	molar flux of reactant i ($mol s)^{-1}$
M_i	molar weight of the reactant i ($kg mol^{-1}$)
n	number of electrons participating in the reaction
p_i	partial pressure of the reactant i (Pa)
P	pressure (Pa)
Q	heat generation in the unit volume of the electrodes ($W m^{-3}$)
R_0	gas constant: 8.314 ($J mol^{-1} K^{-1}$)
R_i	electrical resistance of cell component i (Ω)
T	temperature (K)
$\mathbf{u}$	flow velocity ($m s^{-1}$)
V_{cell}	output voltage of the cell (V)
W_{cell}	volumetric power density of the cell ($W m^{-3}$)
x, y, z	Cartesian coordinates
X_i	molar fraction of the reactant i
Y_i	mass fraction of the reactant i

Greek symbols

ε	porosity of the electrode
η_{act}	activation overpotential (V)
η_{con}	concentration overpotential (V)
η_{ohm}	Ohmic loss (V)
κ	flow permeability in the electrode (m^2)
λ	thermal conductivity ($W m^{-1} K^{-1}$)
μ	viscosity (Pa s)
ρ	density ($kg m^{-3}$)
σ	resisivity (Ω cm)
τ	tortuosity factor of the electrode

Subscripts

an	anode
avr	average
bulk	bulk average in the cross-sectional area of the cell
ca	cathode
ch	fuel channel
ele	electrolyte
gas	gas
gen	generation accompanied by electrochemical reaction
H_2	hydrogen
H_2O	water vapor
IB	interface boundary between solid and porous component of the cell
in	inlet of the cell
int	interconnector
O_2	oxygen
sol	solid
TPB	three-phase boundary

model and discuss the detailed characteristics of flow and reaction fields in the cell. The effects of the design parameters of the cell are surveyed, especially focusing on the cross-sectional configuration and the microstructure of the porous anode. We also propose and assess a simplified numerical model of the anode-supported FT-SOFC for practical design of fuel cell systems [1] based on the knowledge obtained from the 3D simulation.

2. Numerical procedure for three-dimensional simulation

2.1. Computational model

Fig. 1 shows the anode-supported FT-SOFC considered in the present study. As shown in Fig. 1(a), it has a periodic structure in the spanwise (z-) direction. The unit cell is composed of an electrolyte, a cathode, an anode with a fuel channel, an interconnector, and an air channel between the adjacent layers of cells. The thick anode plays a role to mechanically support the cell. The air and fuel flow directions are in co-flow arrangement.

The geometry under computational study is depicted in Fig. 1(b). We take only a half of the unit cell shown in Fig. 1(b), because the flow in each channel is laminar and plane-symmetric since the Reynolds number is low (Re = 1–50) under all operating conditions. The interface between the electrolyte and electrodes are
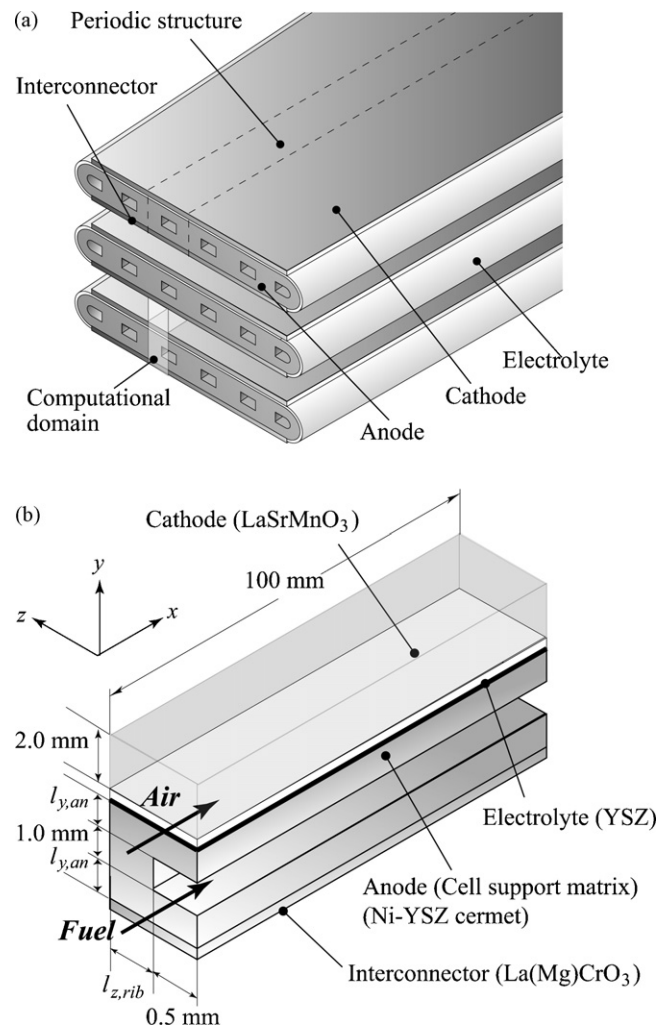

Fig. 1. (a) Schematic of the anode-supported FT-SOFC. (b) Computational model of the anode-supported FT-SOFC. The thin layers of electrolyte, cathode, and interconnector (of which thicknesses are 20 μm, 100 μm and 100 μm, respectively, and treated as boundaries in the simulation) are drawn not in scale so as to be visible.

Table 1
Physical properties of cell components. The values are referring to the previous studies [1,9,12,13]

Component	ρ (kg m^{-3})	C_p (kJ kg^{-1} K^{-1})	λ (W m^{-1}K^{-1})	σ (Ω cm)	ε	τ	d_p (m)
Electrolyte	–	–	2.0	$3.0 \times 10^{-3} \exp(10300/T)$	–	–	–
Cathode	5.62×10^3	0.45	11.0	1.2×10^{-2}	0.5	3.0	1.0
Anode	7.0×10^3	0.45	10.0	$2.98 \times 10^{-3} \exp(-1392/T)$	0.5 or 0.6	Eq. (1)	1.0 or 2.0
Interconnector	–	–	6.0	$5.0 \times 10^{-1} \exp(693.14/T)$	–	–	–

treated as the three-phase boundary (TPB). The electrodes are porous media. The electrolyte and the interconnector are treated as solid boundaries, which couple the fuel and air-sides as described below. The parameters of geometrical configuration to be changed in the present study are the rib width, $l_{z,\mathrm{rib}}$, the rib thickness, $l_{y,\mathrm{an}}$, whereas the width and height of the fuel channel, $l_{z,\mathrm{ch}}$ and $l_{y,\mathrm{ch}}$, are fixed.

The physical properties of each component are listed in Table 1. The resistivity is considered as a function of temperature, whereas other properties are assumed to be constant [1,9,12,13]. Among the material properties of anode, the porosity, $\varepsilon_{\mathrm{an}}$, and the pore diameter, $d_{\mathrm{p,an}}$, are varied in the present study. The tortuosity factor of the porous media, τ, is correlated with the porosity [14]. Note that the tortuosity factor of anode, τ_{an}, used in the previous studies of SOFC has large scatter [4,9,11,15–18]. In the present study, we assume a linear function as follows:

$$\tau_{\mathrm{an}} = 5.0 - 4\varepsilon_{\mathrm{an}}. \tag{1}$$

For the cathode, the porosity and the tortuosity factor ($\varepsilon_{\mathrm{ca}}$ and τ_{ca}) are fixed as $\varepsilon_{\mathrm{ca}} = 0.5$ and $\tau_{\mathrm{ca}} = 3.0$, respectively.

The electrochemical reaction is calculated by using an equivalent circuit as shown in Fig. 2. This model consists of the electromotive force (EMF) and activation overpotential generated in the cell, internal resistance of the cell components and the current path. The cathode and the interconnector are treated as equi-potential surfaces. The average current density of the electrolyte, $i_{\mathrm{ele,ave}}$, which is defined as the current density averaged over the whole area of electrolyte, is kept constant, while the local current density varies in space and is determined as a result of the heat and mass transfer as well as the electrochemical reaction. Since the steady-state performance of the cell is discussed in the present study, the capacitance between the electrolyte and the electrodes is neglected.
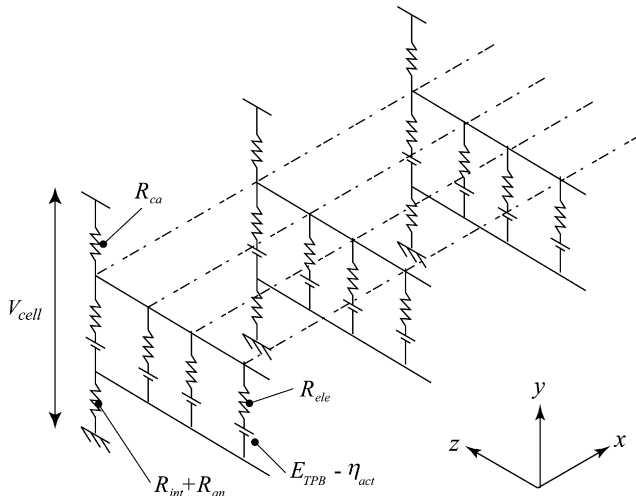

Fig. 2. Equivalent electrical circuit.

2.2. Governing equations and boundary conditions

2.2.1. Momentum transport
The transport equations for mass and momentum are

$$\frac{\partial(\varepsilon\rho)}{\partial t} + \nabla \cdot (\varepsilon\rho\boldsymbol{u}) = 0, \tag{2}$$

$$\frac{\partial(\varepsilon\rho\boldsymbol{u})}{\partial t} + \nabla \cdot \{(\varepsilon\rho\boldsymbol{u})\boldsymbol{u}\} = -\nabla\left(\varepsilon P + \frac{2}{3}\varepsilon\mu\nabla\cdot\boldsymbol{u}\right)$$
$$+ \nabla\cdot[\varepsilon\boldsymbol{\mu}\left\{\nabla u + {}^T(\nabla\boldsymbol{u})\right\}] - \frac{\varepsilon^2\mu}{\kappa}\boldsymbol{u}. \tag{3}$$

These are the volume-averaged conservation equations of mass and momentum in the porous media (see, e.g., [19]). Here, Darcy's law is adopted to describe the superficial flow velocity in the porous media (i.e., the last term in Eq. (3)).

Fully developed laminar velocity profiles are given at the inlets of air and fuel channels. The flow rates are determined by the prescribed air and fuel utilization rates shown in Table 2. The inlet gas pressure, $P_{\mathrm{gas,in}}$, is fixed at 1 atm. Zero-flux boundary condition is applied at the symmetric plane. No-slip boundary conditions are applied on the impermeable boundaries such as the electrolyte and the interconnector.

2.2.2. Transport of chemical species
The transport of chemical species is governed by the following equation:

$$\frac{\partial(\varepsilon\rho Y_i)}{\partial t} + \nabla\cdot(\varepsilon\rho u Y_i) = \nabla\cdot(\varepsilon\rho D_{i,\mathrm{eff}}\nabla Y_i). \tag{4}$$

Here, the effective diffusivity of reactant i in the porous media ($D_{i,\mathrm{eff}}$) is calculated by using the dusty-gas model [4,20], which reads

$$D_{i,\mathrm{eff}} = \frac{\varepsilon}{\tau}\left(\frac{1 - Y_i(1 - \sqrt{M_i/M_{\mathrm{mix}}})}{D_{i,\mathrm{m}}} + \frac{1}{D_{i,\mathrm{k}}}\right)^{-1}, \tag{5}$$

where $D_{i,\mathrm{m}}$ and $D_{i,\mathrm{k}}$ are the multi-component molecular diffusivity and the Knudsen diffusivity of reactant i, respectively, while M_{mix} represents the averaged molar weight of the reactant. Note that $D_{i,\mathrm{m}}$ and $D_{i,\mathrm{k}}$ are functions of the microstructure of the electrode, local temperature, T, and the reactant concentration, Y_i as well as the other physical properties of the fluid [4,15,16,21]. The summation of Eq. (4) for all reactants is identical to Eq. (2).

Methane completely reformed at a steam to carbon ratio of 2.5 is selected as the inlet composition of fuel. Namely, the molar fractions are $X_{\mathrm{H_2,in}} = 8/11$, $X_{\mathrm{H_2O,in}} = 1/11$, and $X_{\mathrm{CO_2,in}} =$

Table 2
Parameters common to all the cases

Inlet gas temperature, $T_{\mathrm{gas,in}}$ (°C)	600
Inlets pressure, $P_{\mathrm{gas,in}}$ (atm)	1.0
O_2 Utilization rate	0.3
H_2 Utilization rate	0.85
Width/height of fuel channel (mm)	1.0
Cell length (mm)	100

2/11, respectively. The corresponding mass fraction is given at the inlet. The boundary condition on the TPB is given by

$$\left.\frac{\partial(\varepsilon\rho Y_i)}{\partial y}\right|_{\text{TPB}} = \pm\frac{i_{\text{ele}}M_i}{nFD_{i,\text{eff}}} \qquad i \in O_2, \ H_2, \ H_2O, \tag{6}$$

where $n = 4$ for O_2 and $n = 2$ for H_2 and H_2O. The sign of the right-hand-side term is plus for O_2 and H_2O, and minus for H_2. The concentration gradient of N_2 and CO_2 on the TPB is assumed to be zero, since these gases are inert. On the interconnector surface, which is impermeable, the concentration gradient of all the reactant should be zero.

2.2.3. Heat transport

The energy transport equation for a porous media as well as for the air and fuel channels is given by using the local equilibrium temperature as:

$$\frac{\partial[\{\varepsilon\rho_{\text{gas}}C_{p,\text{gas}} + (1-\varepsilon)\rho_{\text{sol}}C_{p,\text{sol}}\}T]}{\partial t} + \nabla \cdot (\varepsilon\rho_{\text{gas}}C_{p,\text{gas}}uT)$$
$$= \nabla \cdot [\{\varepsilon\lambda_{p,\text{gas}} + (1-\varepsilon)\lambda_{p,\text{sol}}\}\nabla T] + Q. \tag{7}$$

This is a volume-averaged equation of the heat conduction in the solid part and the energy transport in the fluid phase. The temperature difference between the two phases in the porous electrode can be neglected under the present condition. The local heat production, Q, in Eq. (7) is determined by the local ohmic loss in the electrode.

The solid and porous boundaries at the cell inlet and outlet are assumed to be adiabatic. The inlet gas temperature, $T_{\text{gas,in}}$, is 600 °C throughout the present study unless specified otherwise. We neglect the temperature distribution inside the thin components (i.e., the electrolyte and the interconnector) in the direction of thickness, because they are much thinner than the electrodes and the fluid passages. Namely, the temperatures on both sides, $T_{\text{IB,air}}$ and $T_{\text{IB,fuel}}$ (where the subscript IB denotes the boundary of the electrolyte or interconnector and air and fuel denote the air and fuel sides, respectively) and that in the thin component, T_{sol}, are assumed to be the same, i.e.,

$$T_{\text{IB,air}} = T_{\text{IB,fuel}} = T_{\text{sol}}, \tag{8}$$

and it is computed by solving the following set of equations together with Eq. (8):

$$\begin{cases} q_{\text{air}} = \pm\lambda_{\text{IB,air}}\left.\dfrac{\partial T}{\partial y}\right|_{\text{IB,air}}, \\ q_{\text{fuel}} = \mp\lambda_{\text{IB,fuel}}\left.\dfrac{\partial T}{\partial y}\right|_{\text{IB,fuel}}, \\ q_{\text{air}} + q_{\text{fuel}} = q_{\text{gene}}. \end{cases} \tag{9}$$

Here, λ_{IB} is the thermal conductivity of fluid, while q_{air} and q_{fuel} denote the fractions of q_{gen} distributed to the air and fuel sides, respectively. The heat generation in the unit area of the electrolyte and the interconnector, q_{gen}, is given by

$$\begin{cases} q_{\text{gen,ele}} = i_{\text{ele}}\left[\left(\dfrac{\Delta H_{H_2O}}{2F} - E\right)\right] + \eta_{\text{ohm,ele}} + \eta_{\text{act,ca}} + \eta_{\text{act,an}}, \\ q_{\text{gen,int}} = i_{\text{ele}}\eta_{\text{ohm,int}}, \end{cases} \tag{10}$$

and the division of q_{gen} into q_{air} and q_{fuel} follows the local temperature gradient determined through the iteration between the heat and mass transports and the electrochemical reaction.

2.2.4. Electrochemical reaction

The local current density, i, and the ohmic losses, η_{ohm}, of the cell components are computed by using Ohm's and Kirchhoff's laws

with the values of resistivities, σ, shown in Table 1. The electromotive force (EMF), E, is computed by the Nernst equation, i.e.,

$$E = -\frac{\Delta G_{H_2O}}{2F} + \frac{R_0T}{4F}\ln\left\{\frac{p_{H_2}^2 p_{O_2}}{p_{H_2O}^2}\right\}. \tag{11}$$

The partial pressure of species i, p_i, is obtained as a product of the total local pressure and the molar fraction, X_i, where the molar fraction is calculated by using the mass fraction, Y_i, and the molar weight, M_i, as

$$X_i = \frac{Y_i/M_i}{\sum_j (Y_j/M_j)}. \tag{12}$$

In the present study, the concentration overpotential is defined as the difference between the EMF computed based on the mean concentration, E_{bulk}, and the EMF based on the local concentration on the TPB, E_{TPB}, i.e.,

$$\eta_{\text{con}} = E_{\text{bulk}} - E_{\text{TPB}}$$
$$= \frac{R_0T}{2F}\ln\left\{\frac{(p_{O_2,\text{bulk}}/p_{O_2,\text{TPB}})^{1/2}(p_{H_2,\text{bulk}}/p_{H_2,\text{TPB}})}{(p_{H_2O,\text{bulk}}/p_{H_2O,\text{TPB}})}\right\}. \tag{13}$$

The activation overpotentials in the cathode and anode are implicitly given by the Butler–Volmer equation, i.e.,

$$i_{\text{ele}} = i_o\left\{\exp\left(\frac{\alpha nF\eta_{\text{act}}}{R_0T}\right) - \exp\left(-\frac{(1-\alpha)nF\eta_{\text{act}}}{R_0T}\right)\right\}, \tag{14}$$

where α is the transfer coefficient ($0 < \alpha < 1$) and n is the number of electrons participating in the reaction ($n = 4$ for cathode and $n = 2$ for anode), respectively. In the present study, α is assumed to be 0.5. The exchange current densities, i_o, are expressed as follows [22]

$$\begin{aligned} i_{o,\text{ca}} &= \gamma_{\text{ca}}\left(\frac{p_{O_2,\text{TPB}}}{P}\right)^{1/4}\exp\left(\frac{-E_{\text{act,ca}}}{R_0T}\right), \\ i_{o,\text{an}} &= \gamma_{\text{an}}\left(\frac{p_{H_2,\text{TPB}}}{P}\right)\left(\frac{p_{H_2O,\text{TPB}}}{P}\right)^{-1/2}\exp\left(\frac{-E_{\text{act,an}}}{R_0T}\right), \end{aligned} \tag{15}$$

where γ and E_{act} are the pre-exponential factor and the activation energy of the electrode, respectively. In the present study, the values of these parameters are chosen as shown in Table 3 following the previous studies [9,13,22].

Finally, the output voltage of the cell, V_{cell}, can be obtained by

$$V_{\text{cell}} = E_{\text{bulk}} - (\eta_{\text{con}} + \eta_{\text{ohm}} + \eta_{\text{act}}). \tag{16}$$

2.3. Numerical procedure

Eqs. (2)–(4) and (6) are solved by developing a simulation code based on the standard SMAC procedure [23] under the low-Mach number approximation [24]. Namely, the second-order accurate central difference method is used for the spatial discretization on the staggered mesh system and time integration is done by using the delta-form fractional time step method. The computational grid has a constant spacing in each direction: $\Delta x = 1.5625$ mm, $\Delta y = 0.1000$ mm and $\Delta z = 0.0625$ mm for the air

Table 3
Parameters for activation overpotential. Because γ in Aguiar et al. [13] is given as a function of temperature, the values calculated at $T = 750$ °C are displayed here

	E_{act} (kJ mol^{-1})		γ ($\times 10^9$ A m^{-2})	
	Cathode	Anode	Cathode	Anode
Present study	140	120	5.0	5.0
Campanari et al. [9]	120	110	7.0	7.0
Aguiar et al. [13]	137	140	5.2	28.8
Costamagna et al. [22]	160	140	7.0	0.057

channel and $\Delta x = 1.5625$ mm, $\Delta y = 0.1875$ mm and $\Delta z = 0.0625$ mm for the anode including the fuel channel. The total number of computational cells varies according to the length of each components, i.e., $l_{y,an}$ and $l_{z,rib}$, while the size of each computational cell is kept constant.

The local current density, i, and the ohmic losses, η_{ohm}, that satisfy Ohm's and Kirchhoff's laws with the constitutive Eqs. (11)–(16), are computed by using the Newton-Raphson method. The electrical circuit is segmented on the same mesh as that for the flow simulation (i.e., $\Delta x = 1.5625$ mm and $\Delta z = 0.0625$ mm). Inside the electrolyte and interconnector, electric current in the spanwise direction is neglected.

As mentioned above, the governing equations for the mass, momentum, and energy transports are coupled with those for the electric current via the mass flux on the TPB (Eq. (6)) and the heat production (Q in Eq. (7) and q in Eq. (9)). Iterative computation is continued between the mass, momentum and energy transports and the electric current until the steady-state solution converges for all the variables.

2.4. Validation

In order to validate the numerical procedure described above, we compare the cell performance predicted by the simulation with available experimental data. In most experiments, however, the single cell performance is evaluated in an isothermal furnace and the amount of heat production is negligibly small. Therefore, unlike all other cases in the present study, we neglect the heat production term in Eqs. (7) and (9), but instead assume a uniform temperature of $750\,^\circ$C. The total length of the cell is 100 mm and both height and width of the fuel channel ($l_{y,ch}$ and $l_{z,ch}$) is 1.0 mm. The thicknesses of the cathode and the electrolyte are 100 and 20 μm, respectively. The parameters for the cell structure are assumed as $l_{z,rib}$, = 1.5 mm, $l_{y,an} = 1.0$ mm, $\varepsilon_{an} = 0.5$ and $d_{p,an} = 1.0\,\mu$m.

Fig. 3 shows the relationship between the current and the output voltage (I–V) and also between the current and the power density (I–P) obtained by the present simulation. A fairly good agreement is found with the experimental data [25] when the current density is relatively small, albeit there is some difference in the configuration and operating condition. Larger discrepancy is found for larger current density, i. This discrepancy might have been caused by the strong sensitivity of computational result to the model parameters that cannot be accurately determined from the experiments. For instance, both the I–V and I–P curves nearly collapse with the experimental data when $E_{act,an}$ and the electrolyte thickness $l_{y,ele}$ are adjusted to 130 kJ mol^{-1} and 30 μm, respectively. Another possible cause is the applicability of the thin electrode assumption, which tends to underestimate anodic overpotential when ionic resistance becomes dominant over activation overpotential inside the reactive porous electrode of finite thickness [26].

The grid spacing described above was employed in this validation, and it corresponds to the number of computational cells of $64 \times 21 \times 16$ (in x, y and z directions) for the air-side including the cathode, and of $64 \times 15 \times 16$ for the fuel-side including the anode. Simulation was also performed on a computational grid twice finer in each direction and the resulting change in V_{cell} was within 0.5% difference.

3. Characteristics of transport and reaction phenomena

3.1. Heat and mass transfer

The average current density of the electrolyte, $i_{ele,avr}$, is 0.50 A cm^{-2}. The parameters for the anode structure are set to be $l_{z,rib}$, = 1.5 mm, $l_{y,an} = 1.0$ mm, and $\varepsilon_{an} = 0.5$ and $d_{p,an} = 1.0\,\mu$m. Here-
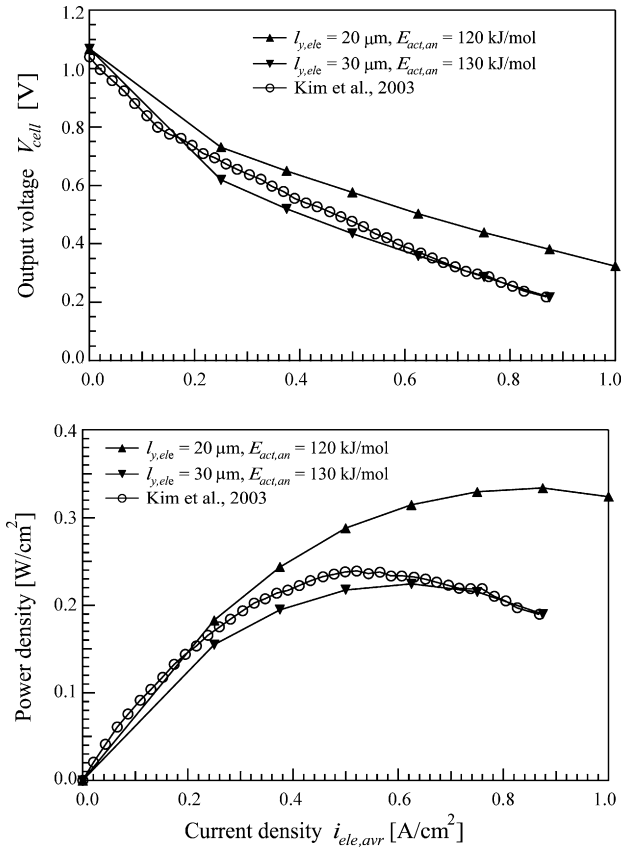
Fig. 3. I–V and I–P characteristics of the isothermal cell ($T = 750\,^\circ$C (constant), $P_{gas,in} = 1.0$ atm).

after, this case is referred to as the reference case. The other common parameters used throughout this study are listed in Table 2.

Fig. 4 shows the distributions of the O_2 concentration on the cathode-side TPB, H_2 and H_2O concentrations on the anode-side TPB, and electrolyte temperature, T_{ele}. Each reactant has a concentration gradient mainly in the streamwise (x) direction, and this is characterized by the rates of consumption and production of each chemical species through the reaction. In addition, concentration gradients of H_2 and H_2O are found also in the spanwise (z) direction, especially on the rib region of the porous anode.

Fig. 5 shows the normalized velocity vector and the molar fractions of H_2 and H_2O in a cross-stream (y–z) plane at $x = 50$ mm. The reactants are transported by the cross-stream flow induced by the migration of O^{2-} ions and the diffusion. The magnitude of this cross-stream flow is $O\,(10^{-2})$ as compared to that of the main stream of fuel. The Péclet number of mass transfer, $Pe_m = UL/D_{i,eff}$, is $O\,(10^{-1})$, where U and L are the maximum velocity of the cross-stream flow and the anode thickness, $l_{y,an}$, respectively. This indicates that the contribution of the cross-stream flow to the mass transfer in the cell is negligibly small compared with that of diffusion in the porous electrodes.

The diffusion paths of the reactants from the air and fuel channels to the TPB are formed in the porous electrodes. Eq. (5) indicates that the magnitude of reactant diffusion inside the electrodes is found to be about ten times smaller than that in the channel region. As a result, variations of H_2 and H_2O concentration are observed in the anode cross-section, which lead the concentration gradient on the TPB. However, the reactant distribution on TPB in the present anode-supported FT-SOFC is less inhomogeneous than that in the conventional anode-supported planar SOFC [6]. This is because the FT-SOFC has the supplementary diffusion paths of the reactants
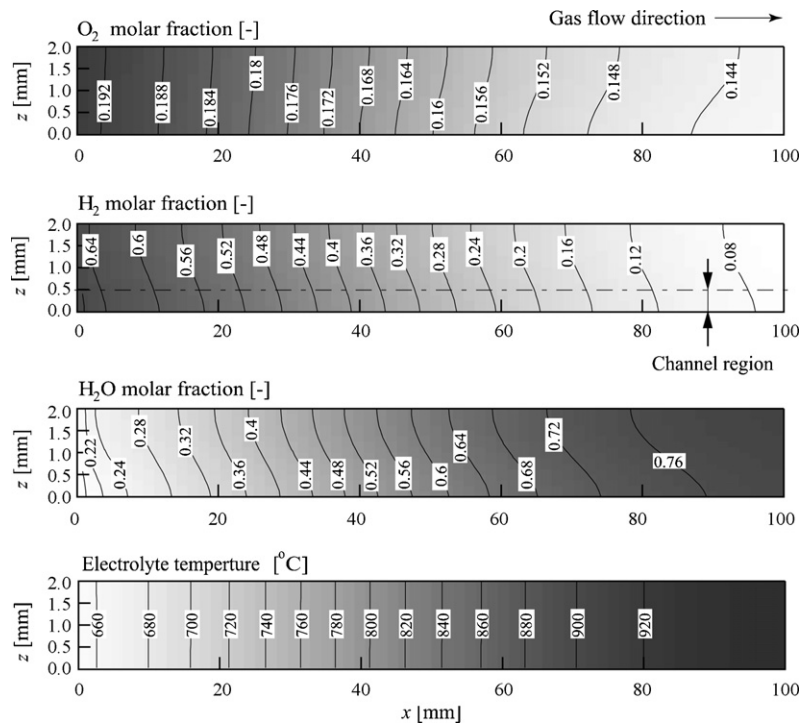
Fig. 4. Molar fraction of O_2, H_2 and H_2O on the TPB and electrolyte temperature (the reference case, $T_{gas,in} = 600\,^\circ C$, $i_{ele,avr} = 0.5\,A\,cm^{-2}$). The gas inlet is located at $x = 0$.
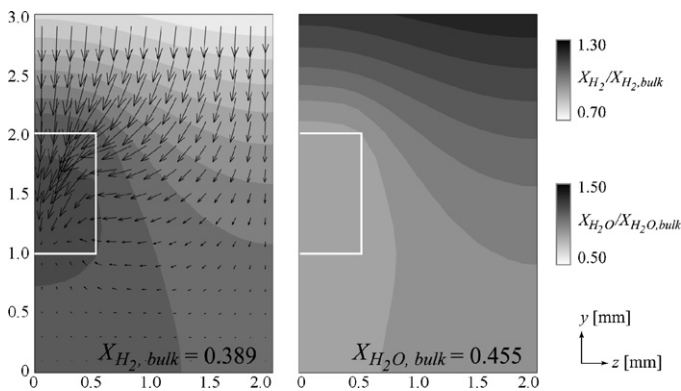

Fig. 5. Normalized velocity vectors and molar fraction of H_2 and H_2O in a cross-section $x = 50\,mm$ (the reference case).

(i.e., the rib of the fuel channel), which do not exist in the planar SOFC.

Since the heat generated by the exothermic reaction is convected by the air and fuel flows, T_{ele} increases monotonously from the cell inlet toward the outlet. The temperature gradient in the cross-sections is small. The temperature distribution is determined mainly by the heat conduction and the local heat production, since the Biot number, $Bi = h_{fuel} l_{y,an} / \lambda_{an}$, is considerably small (less than 0.1 based on the anode thickness). The contribution of the cross-stream flow to the heat transfer in the cell is also small as to the mass transfer, since the Péclet number of heat transfer, $Pe_h = \rho_{gas} C_{p,gas} U L / \lambda_{gas}$, is $O\,(10^{-2})$.

3.2. Electrochemical reaction

Fig. 6 shows the distributions of the electromotive force (EMF), E_{TPB}, and the current density in the electrolyte, i_{ele}. The E_{TPB} takes a maximum at the inlet and gradually decreases toward the cell outlet as O_2 and H_2 are consumed and H_2O is produced. In contrast, the location of maximum i_{ele} appears in the middle of the cell. This is because the overpotentials are very temperature sensitive and there is a trade-off between the increase of temperature and the decrease of reactant concentration. In addition, both E_{TPB} and i_{ele} tend to be smaller in the region above the rib. These characteristics are similar to those of the conventional planar SOFCs with co-flow
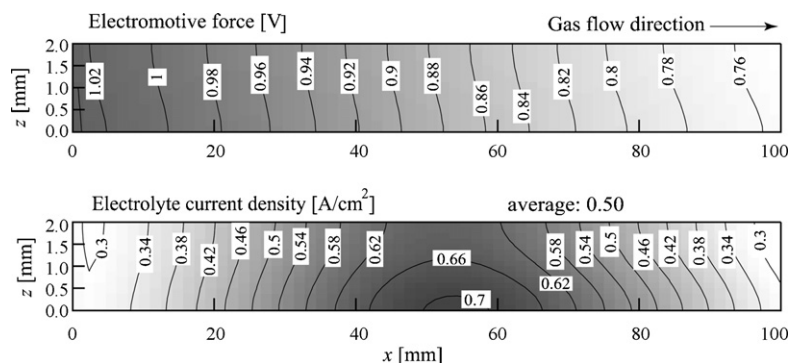

Fig. 6. Electromotive force (EMF) E_{TPB} and electrolyte current density i_{ele} (the reference case).
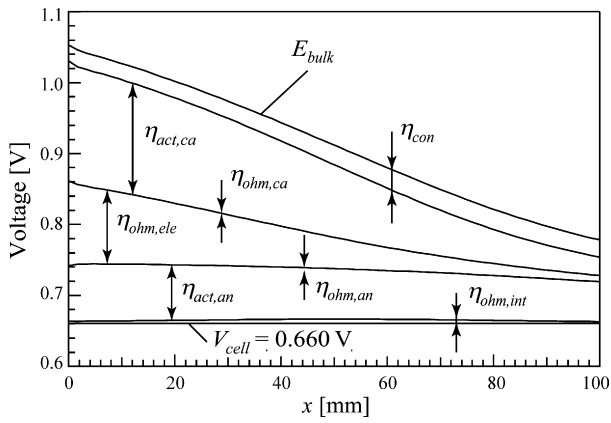
Fig. 7. Distribution of E_{bulk} and spanwise-averaged overpotentials (the reference case).

arrangement, although the spanwise variations of E_{TPB} and i_{ele} are found much smaller [10].

The decrease of E_{TPB} and i_{ele} in the region above the rib is mainly due to insufficient diffusion of H_2 and H_2O in the porous anode. However, as mentioned in Section 3.1, the H_2 shortage and the H_2O stagnation in the anode-supported FT-SOFC can be alleviated by mass transfer through the rib and the bottom of the fuel channel. As a result, the concentration overpotential and the spanwise variations of E_{TPB} and i_{ele} become smaller than those of the conventional planar SOFCs. These characteristics lead to an advantage of FT-SOFC over planar SOFC under the conditions of high fuel utilization.

The componential losses along the streamwise direction are plotted in Fig. 7. It reveals that the dominant components for the voltage loss are the activation overpotential (η_{act}) at the electrodes,

the concentration overpotential (η_{con}), and the ohmic loss of the electrolyte ($\eta_{ohm,ele}$). The ohmic losses of the electrodes ($\eta_{ohm,ca}$ and $\eta_{ohm,an}$) and the interconnector ($\eta_{ohm,int}$) are negligibly small due to their small resistivities. The cathodic activation overpotential ($\eta_{act,ca}$) and $\eta_{ohm,ele}$ are maximized at the cell inlet. This is natural because these losses strongly depend on the temperature and simply decrease as the temperature increases. In contrast, the anodic activation overpotential ($\eta_{act,an}$), which should be determined by the combination of i_{ele}, the local concentrations of H_2 and H_2O, and the temperature, remains almost constant over the streamwise cell length.

3.3. Parametric survey

3.3.1. Effect of the average current density

We examine the condition at which the average current density is a half of the reference case, i.e., $i_{ele,avr} = 0.25\,\mathrm{A\,cm^{-2}}$. The other parameters remain unchanged from the reference case. The resulting output voltage, V_{cell}, is 0.769 V (cf., $V_{cell} = 0.661$ V in the reference case).

Fig. 8 shows the distributions of the electrolyte temperature, T_{ele}, and the local current density, i_{ele}. It is found that the lower $i_{ele,avr}$ makes the temperature higher near the inlet and lower near the outlet. The location of maximum i_{ele} shifts toward upstream with the decrease of $i_{ele,avr}$. The lower temperature near the outlet is simply due to the smaller amount of total heat generation. The higher temperature near the inlet is caused by deterioration of heat exchange, because the air/fuel flow rate changes proportionally to $i_{ele,avr}$ under the condition of constant air/fuel utilization rate.

The concentrations of H_2 and H_2O in the y–z plane at $x = 50$ mm are shown in Fig. 9. Due to the reduced local reaction rate, the concentration gradient in the cross-stream plane is mitigated as
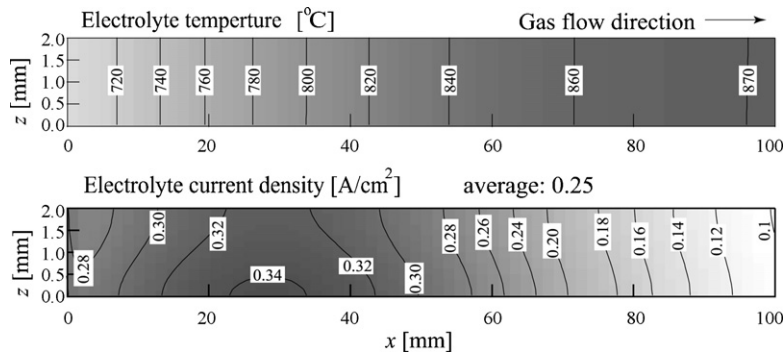

Fig. 8. Electrolyte temperature and current density of the electrolyte with $i_{ele,avr} = 0.25\,\mathrm{A\,cm^{-2}}$.
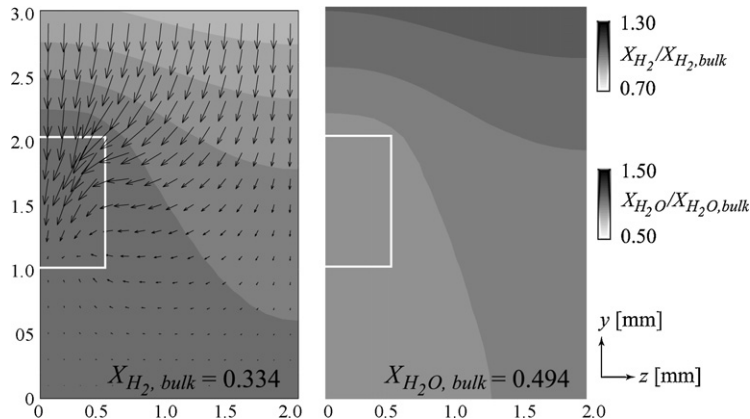

Fig. 9. Normalized velocity vectors and molar fraction of H_2 and H_2O in a cross-section $x = 50$ mm ($i_{ele,avr} = 0.25\,\mathrm{A\,cm^{-2}}$).
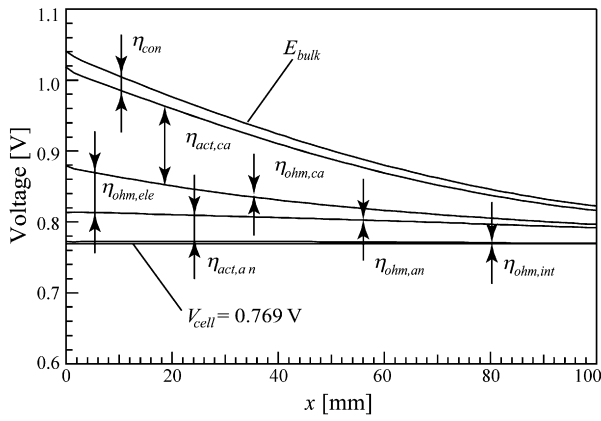
Fig. 10. Distribution of E_{bulk} and spanwise-averaged overpotentials at $i_{ele,avr} = 0.25\,A\,cm^{-2}$.

compared to the reference case. This enhancement of fuel supply leads to the smaller spanwise variation of i_{ele}, as is observed in Fig. 8, and the smaller concentration gradient decreases both η_{con} and $\eta_{act,an}$ as shown in Fig. 10. Moreover, the lower $i_{ele,avr}$ and the higher temperature near the inlet result in the decrease of η_{act}, both for the anode and the cathode, and also of $\eta_{ohm,ele}$. As a combination of these effects, the output voltage increases with the decrease of $i_{ele,avr}$.

3.3.2. Effect of the design parameter

Several cases with different design parameters of the anode, i.e., the pore diameter, $d_{p,an}$, the porosity, ε_{an}, the rib width, $l_{z,rib}$, and the rib thickness, $l_{y,an}$, are studied. Table 4 summarizes the resulting output voltage, V_{cell}, for these cases. As compared to the reference case, V_{cell} is significantly improved in the case of larger $d_{p,an}$, while only marginally higher in the other cases studied.

The increase of V_{cell} is explained by the mass transfer enhancement in the cross-sectional plane as shown in Fig. 11. In all cases, the fuel concentration in the porous anode becomes uniform and that on the TPB is larger than the reference case. This enhanced diffusion improves the supply of H_2 and mitigates the stagnation of H_2O, so that η_{con} and $\eta_{act,an}$ are reduced. In the cases of larger $d_{p,an}$ or ε_{an}, the enhancement of diffusion is attributed to the increase of the effective diffusivity, $D_{i,eff}$. As suggested by Eq. (5), $D_{i,eff}$ increases with increase of $d_{p,an}$, because the Knudsen diffusivity, $D_{i,k}$, is proportional to $d_{p,an}$. Eq. (5) also indicates that $D_{i,eff}$ increases as ε_{an} is increased. On the other hand, for the anode with a thinner or narrower rib, shorter diffusion length directly results in the enhancement of mass transfer, although $D_{i,eff}$ is unchanged.

Fig. 12 shows the distribution of the electrolyte temperature. The boundary and operating conditions are to the same as those of refer-

ence case. The temperature drops with the increase of ε_{an}, whereas it is almost unchanged by the variation of $d_{p,an}$. As discussed in Section 3.1, the heat transfer in the porous anode is dominated by the streamwise heat conduction. It is nearly proportional to the cross-sectional area, S_{an}, and the effective thermal conductivity, λ_{eff}, which is defined as

$$\lambda_{eff} = \varepsilon\lambda_{gas} + (1 - \varepsilon)\lambda_{sol}. \tag{17}$$

Therefore, the observation in each case can be explained as follows:

- For larger pore ($d_{p,an} = 2.0\,\mu m$):
  The temperature distribution is unchanged because S_{an} and λ_{eff} are independent of $d_{p,an}$.
- For higher porosity ($\varepsilon_{an} = 0.6$):

The heat conduction is reduced because λ_{gas} is much smaller than λ_{sol}. The reduced heat conduction causes the temperature drop and the increase of η_{act} and $\eta_{ohm,ele}$ near the inlet. The deterioration due to this temperature drop is nearly canceled by the favorable effect due to the mass transfer enhancement discussed above.

Fig. 12 also shows that the inlet temperature decreases with the decrease of $l_{z,rib}$ and $l_{y,an}$. When the rib is thin or narrow, the streamwise heat conduction is suppressed due to the reduction of the cross-sectional area. This leads to the decrease of inlet temperature and the increase of η_{act} and $\eta_{ohm,ele}$, similarly to the case of large ε_{an}. In these cases, the decrement of cross-sectional area is comparable to that of diffusion length. Thus, a trade-off occurs between the mass transfer enhancement and the heat conduction degradation when $l_{z,rib}$ and $l_{y,an}$ are varied. As a result, V_{cell} is relatively insensitive to these parameters.

In the present study, the activation overpotential model, Eq. (15) is fixed during the parametric survey of the anode microstructure, i.e., $d_{p,an}$, and ε_{an}. However, recent efforts have shown that introducing thin anode functional layer can improve both activation and concentration overpotentials [27–29]. Besides, it is estimated that the effective anode reactive thickness for standard grain size (1 μm) is around 10 μm [30], which is much smaller than the total anode thickness. Thus, it seems reasonable to assume thin active layer and to optimize bulk anode support layer independently without changing the activation overpotential at the anode electrolyte interface.

4. Development of simplified cell model

4.1. Model description

In this section, a simplified numerical model for the anode-supported FT-SOFC is developed based on the knowledge obtained by the 3D simulation presented above. The results of 3D simula-

Table 4
Dependency of V_{cell} on $i_{ele,avr}$ and anode design parameters obtained by 3D and simplified simulations

Case	Reference case	Lower current	Larger pore	Higher porosity	Narrower rib	Thinner anode
Parameters						
Average current density $i_{ele,avr}$ (A cm^{-2})	0.50	**0.25**	0.50	0.50	0.50	0.50
Pore diameter $d_{p,an}$ (μm)	1.0	1.0	**2.0**	1.0	1.0	1.0
Porosity ε	0.5	0.5	0.5	**0.6**	0.5	0.5
Rib width $l_{z,rib}$ (mm)	1.5	1.5	1.5	1.5	**0.5**	1.5
Thickness $l_{y,an}$ (mm)	1.0	1.0	1.0	1.0	1.0	**0.4**
Computed output voltage, V_{cell}						
3D simulation (V)	0.660	0.769	0.687	0.676	0.668	0.666
Simplified simulation (V)	0.691	0.769	0.698	0.689	0.696	0.686

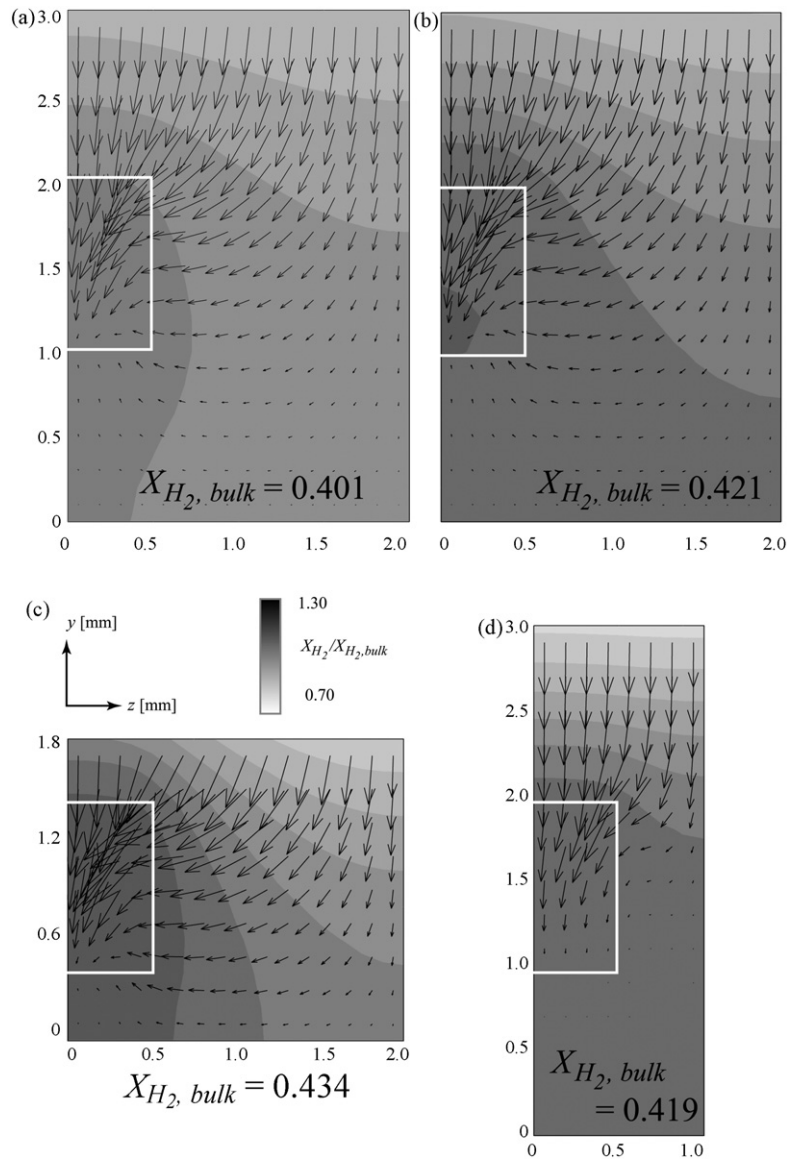Values in bold are differences from those of the reference case.

Fig. 11. Normalized velocity vectors and molar fraction of H$_2$ in a cross-section $x = 50$ mm under different design parameters: (a) larger pore; (b) higher porosity; (c) thinner anode; (d) narrower rib. See, Table 4 for the specification of each case.
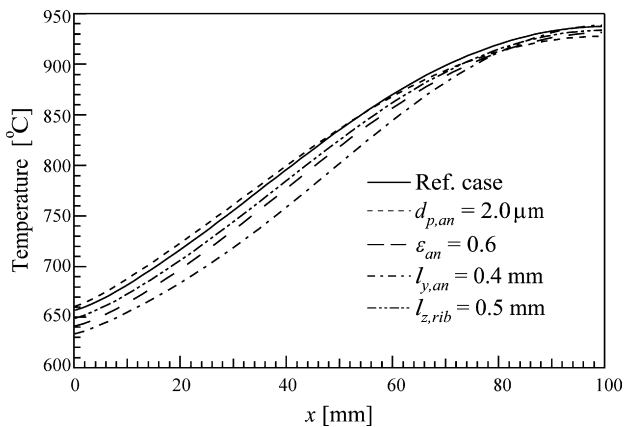

Fig. 12. Electrolyte temperature under different design parameters ($i_{ele,avr} = 0.5$ A cm^{-2}).

tion confirm that lateral (z) variation of the reaction field at TPB for the anode-supported FT-SOFC is very small, and the advection terms of the transport equations can be neglected. Namely, the distribution of the electrochemical field (i.e., current density, EMF, and overpotentials) at TPB can be assumed to be uniform in the spanwise direction, and the air and fuel streams to be one-dimensional plug flows. The resulting model is basically similar to the conventional one-dimensional model [11,13,15,31,32]. In this model, a special procedure is adopted to treat the concentrations of H$_2$ and H$_2$O in the thick anode with a complex cross-sectional geometry.

The cell is divided into six segments, as shown in Fig. 13(a). These segments as well as the air and fuel channels are discretized by control volumes in the streamwise (x) direction. The physical quantities, i.e., the mass flux of each species and the temperature, are defined at each control volume. The solution for the set of conservation equations (described in the following sections) is obtained by using the Newton-Raphson method.
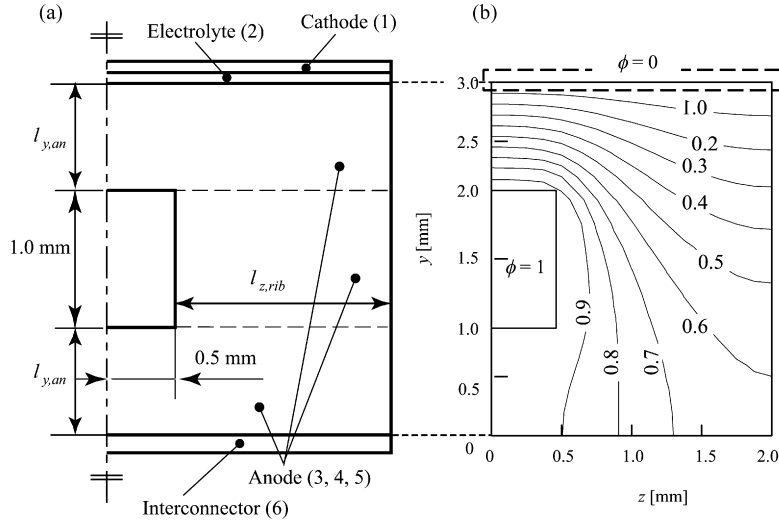
Fig. 13. (a) Segmented component model of the anode-supported FT-SOFC. (b) Distribution of ϕ in the cross-sectional area of the anode and fuel channel (Reference case). The thin layers of electrolyte, cathode, and interconnector (of which thicknesses are 20 μm, 100 μm and 100 μm, respectively, and treated as boundaries in the simulation) are drawn not in scale so as to be visible.

4.1.1. Transport in fuel and air channels

The transports of the mass-flux of each reactant, $\bar{m}_j$, and the temperature, T, in the fuel and air channels are expressed as

$$
\begin{cases}
\dfrac{\partial \bar{m}_j}{\partial x} = \pm (l_{z,\text{ch}} + l_{z,\text{rib}}) \dfrac{i_{\text{ele}}}{n_i F} & j \in O_2, H_2, H_2O \\
\dfrac{\partial \bar{m}_j}{\partial x} = 0 & j \in N_2, CO_2
\end{cases}
\tag{18}
$$

and

$$
\frac{\partial}{\partial x}\left[\left(\sum_j \bar{m}_j c_{p,j} \right) T_{\text{gas}} \right] dx = q_{\text{cond}} + q_{\text{conv},x} + q_{\text{conv},y} + q_{\text{ht}}
\tag{19}
$$

air side : $\quad j \in N_2, O_2 \quad k \in O_2$
fuel side : $\quad j \in H_2, H_2O, CO_2 \quad k \in H_2, H_2O,$

where

$$
q_{\text{cond}} = A_{\text{ch}} \left[\frac{\partial}{\partial x}\left(\lambda_{\text{gas}} \frac{\partial T_{\text{gas}}}{\partial x} \right) \right] dx,
\tag{20}
$$

$$
q_{\text{conv},x} = A_{\text{ch}} \frac{\partial}{\partial x}\left[\sum_j \bar{m}_j \int^T c_{p,j}\, dT \right] dx,
\tag{21}
$$

$$
q_{\text{conv},y} = (l_{z,ch} + l_{z,\text{rib}}) dx \sum_k \frac{\pm i_{\text{ele}}}{n_k F} \int^T c_{p,k} T,
\tag{22}
$$

$$
q_{\text{ht}} = A_{\text{ht}} h (T_{\text{gas}} - T_{\text{sol}}).
\tag{23}
$$

Here, A_{ch} and A_{ht} are the cross-sectional area of the flow channel and the area that participate in the convective heat transfer, respectively. Each term on the right hand side of Eq. (19) expresses the heat conduction, the convective heat transfer, and the heat convection on the TPB. In order to determine the heat transfer coefficient, h, in Eq. (23), the Nusselt number for the parallel plates ($Nu_H = 8.235$) and that for the square duct ($Nu_H = 3.599$) [33] are used for the air and fuel channels, respectively.

4.1.2. Transport in solid and porous elements

As mentioned in the Section 3.1, the Péclet number of heat transfer in each cross-sectional area of the cell is considerably small. In addition, the main streams of air and fuel hardly affect the heat transfer inside the electrodes. Namely, the heat transfer in the electrodes is governed by the heat conduction only. With this assumption, the heat transport in the element j (see, Fig. 13(a)) can be expressed as

$$
A_{xcj} \left[\frac{\partial}{\partial x}\left(\lambda_{\text{eff},j} \frac{\partial T_{\text{sol},j}}{\partial x} \right) \right] dx = q_{\text{ht},j} + \sum_k q_{\text{cond},j,k} + q_{\text{gene},j},
\tag{24}
$$

where

$$
q_{\text{ht},j} = \begin{cases} A_{\text{ht},j} h (T_{\text{gas}} - T_{\text{sol},j}) & j \in 1, 3, 4, 5, 6 \\ 0 & j \in 2 \end{cases}
\tag{25}
$$

$$
q_{\text{gene}} = \begin{cases} i_j A_{y,j} \eta_{\text{ohm},j} & j \in 1, 3, 4, 5, 6 \\ i_j A_{y,j} \left[\left(-\dfrac{\Delta H_{H_2O}}{2F} - E \right) + (\eta_{\text{ohm},j} + \eta_{\text{act}}) \right] & j \in 2 \end{cases}
\tag{26}
$$

and

$$
q_{\text{cond},j,k} = \frac{A_{y,j,k}}{(\delta_j / \lambda_{\text{eff},j}) + (\delta_k / \lambda_{\text{eff},k})} \frac{\partial T_{\text{sol}}}{\partial y}.
\tag{27}
$$

Here, $A_{x,j}$ and $A_{y,j}$ are the areas of heat transmission in the streamwise and perpendicular directions, respectively, and δ_j is the thickness of the component j. In Eq. (24), the electrodes are treated as solid with an effective heat conductivity of λ_{eff}. The summation of Eq. (25) for j is equivalent to Eq. (23). Note that the effect of the anode design can be investigated by changing the parameters of microstructure, ε_{an} and $d_{\text{p,an}}$, and the size of elements 3, 4 and 5 shown in Fig. 13(a).

4.1.3. Concentration of reactant on TPB

In the conventional models, the molar concentration that participates in the electrochemical process at the TPB is given by

$$
X_{i,\text{TPB}} = X_{i,\text{ch}} \pm \frac{i_{\text{ele}}}{nF} \frac{R_0 T}{P D_{i,\text{eff}}} \frac{1}{l_{\text{diff}}},
\tag{28}
$$

where n is the number of electrons in the reaction, while l_{diff} is the diffusion length being equal to the anode thickness in the case of planar SOFC [34]. However, l_{diff} cannot be determined for arbitrary cross-sectional geometry. Also, as observed in Figs. 5, 9 and 11, variations of H_2 and H_2O concentrations in the cross-section of anode cannot be neglected. Hence, the following procedure is employed to obtain the spanwise-averaged concentration of reactants on the TPB.

We assume that the physical properties are constant in the cross-section and that the concentration variation in the streamwise direction is much milder than that in the cross-section. Then,

the transport equation for the species, Eq. (4), reduces to the two-dimensional Laplace equation by neglecting the advection term, i.e.,

$$\frac{\partial^2 \phi}{\partial y^2} + \frac{\partial^2 \phi}{\partial z^2} = 0. \tag{29}$$

Here, the normalized mass fraction, ϕ, is defined as

$$\phi(y, z) = \frac{Y_i(y, z) - Y_{i,\mathrm{TPB}}}{Y_{i,\mathrm{ch}} - Y_{i,\mathrm{TPB}}}, \tag{30}$$

with $Y_{i,\mathrm{ch}}$ and $Y_{i,\mathrm{TPB}}$ being the mass fractions of reactant i in the flow channel and that on the TPB, respectively. This Laplace equation is solved with boundary conditions of $\phi = 1$ in the fuel channel and $\phi = 0$ on the TPB. The spanwise (z-) gradient of ϕ is zero on the symmetric planes (i.e., for anode-side, $\partial\phi/\partial z = 0$ at $z = 0$ mm and $z = 2$ mm in Fig. 13(b)). Once Eq. (29) is solved for ϕ, as exemplified in Fig. 13(b), the gradient of Y_i at the TPB can be computed as

$$\left.\frac{\partial Y_i}{\partial y}\right|_{\mathrm{TPB}} = (Y_{i,\mathrm{ch}} - Y_{i,\mathrm{TPB}}) \left.\frac{\partial \phi}{\partial y}\right|_{\mathrm{TPB}}. \tag{31}$$

With an assumption of constant physical property, the molar fraction of reactant i on the TPB can be computed by using Eqs. (6), (12), (31) and the gas state equation, as

$$X_{i,\mathrm{TPB}} = X_{i,\mathrm{ch}} \pm \frac{i_{\mathrm{ele}}}{nF} \frac{R_0 T}{PD_{i,\mathrm{eff}}} \left(\left.\frac{\partial \phi}{\partial y}\right|_{\mathrm{TPB}}\right)^{-1}. \tag{32}$$

The normalized concentration gradient on the TPB $(\partial\phi/\partial y)|_{\mathrm{TPB}}$, depends only on the cross-sectional geometry of the cell and it can be obtained by solving the Laplace equation only once for the given geometry. Note that Eq. (32) is equivalent to Eq. (28) for the cathode-side, if $1/(\partial\phi/\partial y)_{\mathrm{TPB}}$ is replaced by $l_{y,\mathrm{ca}}$.

4.1.4. Electrochemical reaction

The governing equations and numerical scheme for the electrochemical reaction is the same as in the case of 3D simulation. The only difference in the simplified model is the spanwise-averaged equivalent circuit model, which has a single current path in a set of electrolyte and electrodes.
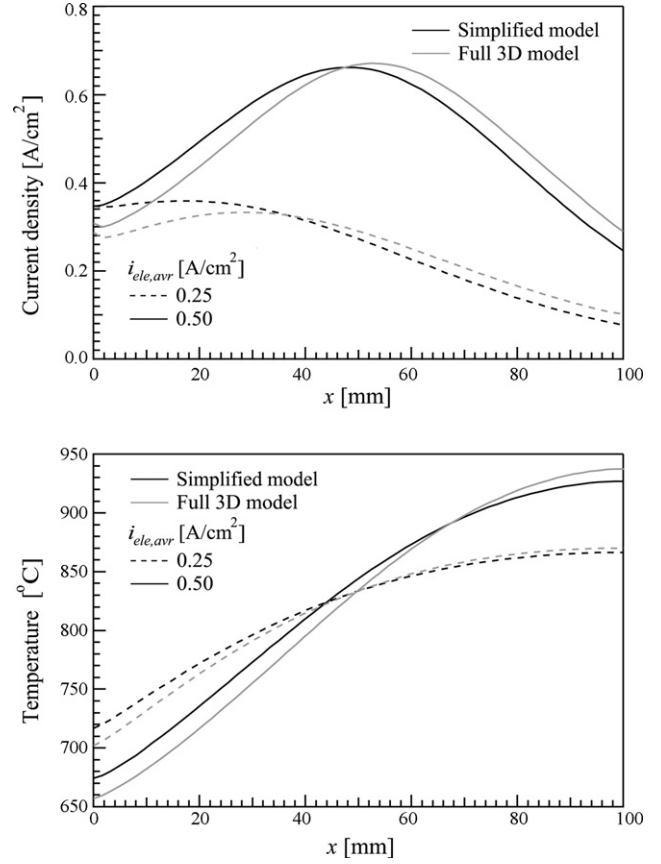

Fig. 14. Temperature and current density at $i_{\mathrm{ele,avr}} = 0.25$ and $0.50\,\mathrm{A\,cm^{-2}}$ (reference case).

4.2. Validation of the model

Fig. 14 shows the distributions of i_{ele} and T_{ele} predicted by the simplified model in the cases of $i_{\mathrm{ele,avr}} = 0.25$ and $0.5\,\mathrm{A\,cm^{-2}}$ (reference case). The profiles computed by using the simplified model are
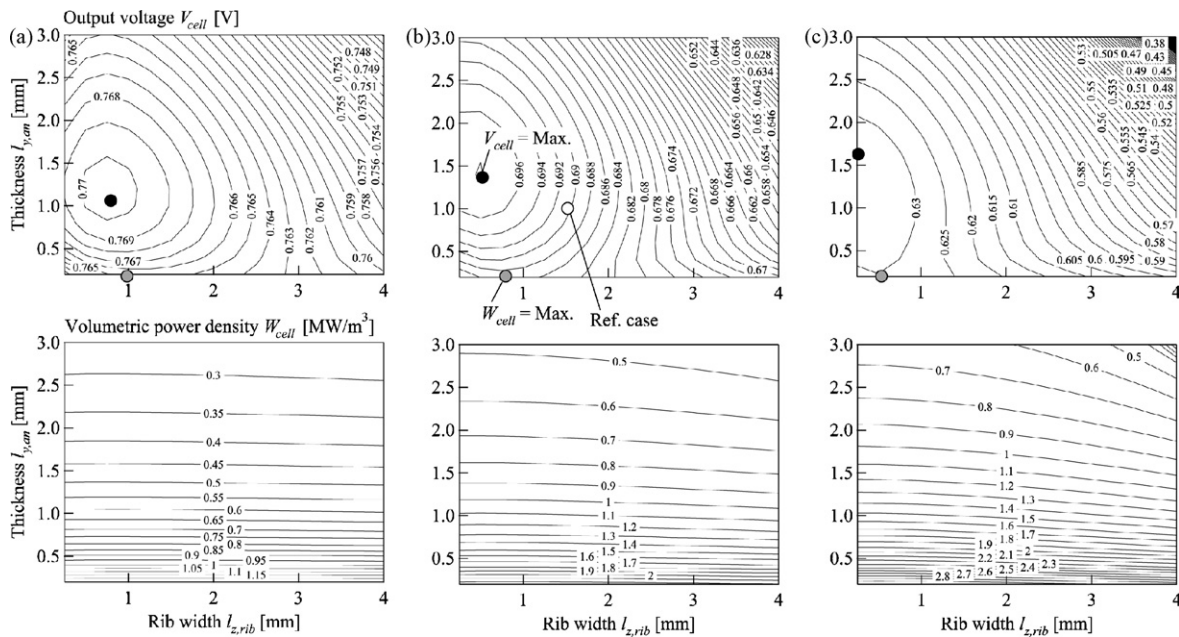

Fig. 15. Output voltage (upper row) and volumetric power density (lower row) for wide range of parameters: (a) $i_{\mathrm{ele,avr}} = 0.25\,\mathrm{A\,cm^{-2}}$; (b) $i_{\mathrm{ele,avr}} = 0.50\,\mathrm{A\,cm^{-2}}$; (c) $i_{\mathrm{ele,avr}} = 0.75\,\mathrm{A\,cm^{-2}}$. The open circle in (b) corresponds to the reference case.

in good agreement with those of 3D simulations. In the reference case, the deviations from the 3D simulation are within $9\,\mathrm{mA\,cm^{-2}}$ for the maximum current density, $10.4\,\mathrm{K}$ for the maximum temperature, and within 5 mm for the peak location of current density. This difference may be due to the assumptions of constant Nusselt number and spanwise uniformity of the reaction rate. The Nusselt number is much larger in the thermal-entry region [35], of which length is increased with increase of $i_{\mathrm{ele,avr}}$. The assumption of constant Nusselt number results in overprediction of the temperature near the inlet and underprediction of the overpotential. On the other hand, as discussed in Section 3.3, the spanwise variation of i_{ele} is pronounced when the mass diffusion is insufficient. Namely, the assumption of uniform reaction rate might have caused the errors in η_{con}, η_{act} and i_{ele}.

The resulting output voltage, V_{cell}, is shown in Table 4 for different values parameters. Although the computed voltage is in fair agreement with the 3D simulation, discrepancy is also found depending on the parameters. Agreement with the 3D model is found to be better for cells with a thick anode with narrow rib, in which the spanwise variation of reaction is relatively small. The computational cost of this simplified model is $1/10^5$ that of the 3D simulation. These results suggest that present simplified model of the anode-supported FT-SOFC can be used as a convenient tool for the parametric survey of cell design and operating conditions.

4.3. Example application

As an example application of the simplified model, we perform a parametric survey with wide ranges of anode thickness, $l_{y,\mathrm{an}}$ (from 0.2 to 3.0 mm with increment of 0.2 mm), rib width, $l_{z,\mathrm{rib}}$ (0.25 to 4.00 mm with increment of 0.25 mm), and average current density, $i_{\mathrm{ele,avr}}$ (0.25, 0.5 and 0.75 A cm^{-2}). All other parameters are assumed to be the same as those of the reference case.

Fig. 15 shows the computed voltage, V_{cell}, and the volumetric power density, W_{cell}, defined as

$$W_{\mathrm{cell}} = \frac{V_{\mathrm{cell}} i_{\mathrm{ele,avr}}}{l_{y,\mathrm{cell}}}, \qquad (33)$$

where $l_{y,\mathrm{cell}}$ is the cell thickness, which is the summation of electrolyte, electrodes and interconnector thicknesses. As can be noticed from this figure, we can find a set of parameters to attain desired performance by using the present simplified model: for instance $(l_{y,\mathrm{an}}, l_{z,\mathrm{rib}}) = (1.4, 0.5\,\mathrm{mm})$ for the maximum V_{cell} at $i_{\mathrm{ele,avr}} = 0.5\,\mathrm{A\,cm^{-2}}$, and $(l_{y,\mathrm{an}}, l_{z,\mathrm{rib}}) = (0.2, 0.8\,\mathrm{mm})$ for the maximum W_{cell} at $i_{\mathrm{ele,avr}} = 0.5\,\mathrm{A\,cm^{-2}}$.

5. Conclusions

Numerical simulation and modeling of the heat/mass transfer and electrochemical reaction in an anode-supported flat-tube solid oxide fuel cell (FT-SOFC) are carried out. Through the numerical analyses with a parametric survey, the following conclusions are derived:

1. The distributions of the reaction fields in the anode-supported FT-SOFC are quantitatively similar to those of the conventional planar cell with co-flow arrangement. However, the concentration and activation overpotentials are mitigated in FT-SOFC by enhanced reactant diffusion in the porous rib of the fuel channel. These characteristics give an advantage to FT-SOFC over planar SOFC under the condition of high fuel utilization and high current density.
2. The design parameters affect the performance characteristics as well as flow field of the cell. For a fixed activation overpotential model, a higher output voltage is obtained by using an anode with larger pore diameter. However, the output voltage of the cell is less sensitive to the cross-stream geometry of anode due to a trade-off between the heat transfer and the mass transfer.
3. A simplified numerical model of the anode-supported FT-SOFC is developed based on the results obtained by the three-dimensional simulation. This model can predict sufficiently well the output voltage as well as the distributions of temperature and current density with very low computational cost. Thus, it can be used as a convenient tool for surveying wide range of anode support FT-SOFC design parameters. In order to determine the optimal design of the anode-supported FT-SOFC, however, further parametric survey should be required.

References

[1] S.C. Singhal, K. Kendall, High Temperature Solid Oxide Fuel Cell: Fundamentals, Design, and Applications, Elsevier Advanced Technology, Oxford, 2003.
[2] G. DiGiuseppe, Proceedings of the 9th International Symposium on Solid Oxide Fuel Cell, 2005, pp. 322–332.
[3] A.K.S. Iyengar, G. DiGiuseppe, N. Desai, S. Vora, L. Shockling, Proceedings of the 4th International Conference Fuel Cell Science Engineering and Technology, 2006 (FUELCELL2006-97053).
[4] H. Yakabe, M. Hishinuma, M. Uratani, Y. Matsuzaki, I. Yasuda, J. Power Sources 86 (2000) 423–431.
[5] J. Yuan, M. Rokni, B. Sundén, Int. J. Heat Mass Transfer 46 (2003) 809–821.
[6] Y.N. Magar, R.M. Manglik, J. Fuel Cell Sci. Technol. 4 (2007) 185–193.
[7] B.A. Haberman, J.B. Young, Int. J. Heat Mass Transfer 47 (2004) 3617–3629.
[8] P.W. Li, M.K. Chyu, J. Heat Trans. 124 (2005) 219–229.
[9] S. Campanari, P. Iora, J. Power Sources 132 (2004) 113–126.
[10] H. Yakabe, T. Ogiwara, M. Hisinuma, I. Yasuda, J. Power Sources 102 (2001) 144–154.
[11] S.H. Chan, K.A. Khor, Z.T. Xia, J. Power Sources 93 (2001) 130–140.
[12] V.V. Kharton, F.M.B. Marques, A. Atkinson, Solid State Ionics 174 (2004) 135–149.
[13] P. Aguiar, C.S. Adjiman, N.P. Brandon, J. Power Sources 138 (2004) 120–136.
[14] S.C. Carniglia, J. Catal. 102 (1986) 401–418.
[15] H. Zhu, R.J. Kee, J. Power Sources 117 (2003) 61–74.
[16] Y. Ji, K. Yuan, J.N. Chung, Y.C. Chen, J. Power Sources 161 (2006) 380–391.
[17] W.G. Bessler, S. Gewies, J. Warnatz, Proceedings of the 9th International Symposium on Solid Oxide Fuel Cell (2005) 708–718.
[18] R.E. Williford, L.A. Chick, G.D. Maupin, S.P. Simner, J.W. Stevenson, J. Electrochem. Soc. 150 (2003) A1067–A1072.
[19] K. Vafai, Thiyagaraja, Int. J. Heat Mass Transfer 30 (1987) 1391–1405.
[20] R. Suwanwarangkul, E. Croiset, M.W. Fowler, P.L. Douglas, E. Entchev, M.A. Douglas, J. Power Sources 122 (2003) 9–18.
[21] R.B. Bird, W.E. Stewart, E.N. Lightfoot, Transport Phenomena, 2nd ed., John Wiley and Sons, New York, 2002.
[22] P. Costamagna, K. Honegger, J. Electrochem. Soc. 145 (1998) 3995–4007.
[23] A.A. Amsden, F.H. Harlow, Los Alamos Report, (1970) LA-4370.
[24] A. Majda, J. Sethian, Combust. Sci. Technol. 42 (1985) 185–205.
[25] J.H. Kim, R.H. Song, K.S. Song, S.H. Hyun, D.R. Shin, H. Yokokawa, J. Power Sources 122 (2003) 138–143.
[26] P. Costamagna, P. Costa, V. Antonucci, Electrochim. Acta 43 (1998) 375–394.
[27] E. Wanzenberg, F. Tietz, P. Panjan, D. Stöver, Solid State Ionics 159 (2003) 297–308.
[28] R.N. Basu, G. Blass, H.P. Buchkremer, D. Stöver, F. Tietz, E. Wessel, I.C. Vinke, J. Eur. Ceram. Soc. 25 (2005) 463–471.
[29] S.D. Kim, S.H. Hyun, J. Moon, J.-H. Kim, R.H. Song, J. Power Sources 139 (2005) 67–72.
[30] J.H. Nam, D.H. Jeon, Electrochim. Acta 51 (2006) 3446–3460.
[31] J.R. Ferguson, J.M. Fiard, R. Herbin, J. Power Sources 58 (1996) 109–122.
[32] M. Iwata, T. Hikosaka, M. Morita, T. Iwanari, K. Ito, K. Onda, Y. Esaki, Y. Sakaki, S. Nagata, Solid State Ionics 132 (2000) 297–308.
[33] R.K. Shah, A.L. London, in: T.F. Irvine Jr., J.P. Hartnett (Eds.), Laminar Flow Forced Convection in Ducts, Academic press, New York, 1978 (Supplement 1 of Advances in Heat Transfer).
[34] J.W. Kim, A.V. Virkar, K.Z. Fung, K. Mehta, S.C. Singhal, J. Electrochem. Soc. 146 (1999) 69–78.
[35] W. Kays, M. Crawford, B. Weigand, Convective Heat and Mass Transfer, 4th ed., McGraw Hill, New York, 2005.